COMPARISONS OF COMPUTED AND EXPERIMENTAL PRESSURES FOR TRANSONIC FLOWS ABOUT ISOLATED WINGS AND WING–FUSELAGE CONFIGURATIONS

By F. R. Bailey
NASA Ames Research Center

and

W. F. Ballhaus
U.S. Army Air Mobility R&D Laboratory

INTRODUCTION

Most modern aircraft achieve optimum cruise performance and maneuverability when flying at high subsonic Mach numbers in the transonic regime. In this Mach number range, there exist in the flow field local regions of supersonic flow which are usually terminated by weak embedded shock waves. These mixed subsonic–supersonic flows are extremely sensitive to the shape of internal boundaries. For this reason aircraft performance depends strongly on aircraft configuration. The configuration design process requires parametric variation of the numerous geometrical variables that describe the shape of the aircraft, a procedure that is expensive to implement entirely by experiment. This fact has resulted in a significant effort to develop theoretical transonic flow analysis methods.

These theoretical techniques can be divided into two categories: (1) analytical methods and (2) numerical methods. The analytical approach is limited, in the general case, to linear theory, while most transonic flows of interest are governed by nonlinear equations of motion. The numerical approach, however, has no such limitation.

The present work describes a relaxation procedure for solving the transonic small disturbance equation for flows about wings and wing-fuselage combinations. The numerical method is based on the well-known relaxation method of Murman and Cole (ref. 1) and is a continuation of the work given by Ballhaus and Bailey (refs. 2 and 3; see also ref. 4). The small disturbance formulation is chosen because of the relatively simple manner in which the wing boundary condition is imposed. All the transonic relaxation methods for wings that have been developed to date (refs. 2 to 10) are based on the small disturbance approach, with the exception of Jameson's (ref. 11) method for yawed wings. In the present method, solutions are obtained over a sequence of successively refined computational grids with the final result obtained for a grid with about 10^5 points. The solution process requires about 5 to 15 min of run time on a Control Data Corporation (CDC) 7600 computer.

An early version of the isolated wing code was released to aircraft and research companies in 1974. Since that time, in a contracted effort with LTV Aerospace Corporation, the input, setup, and output have been streamlined

and adapted more toward the needs of the aircraft designer. The code has been documented and adapted for use on the CDC 6600 computer (ref. 12). The solution process has also been revised to decrease computer run time and to allow, as an option, either conservative or nonconservative differencing. The use of conservative differencing ensures that captured shock waves satisfy the shock conditions contained in the inviscid governing equation. Such is not the case for nonconservative differencing which, coincidentally, captures shock waves that agree better with experimentally measured shock waves which, of course, are affected by viscosity. (See ref. 13, fig. 6.) Computed surface pressures for both conservative and nonconservative differencing are compared with experimental pressures in the section on results.

Finally, the method has been extended for the treatment of wings mounted on finite length fuselages. Results, both conservative and nonconservative, are compared with experimental data for two such nonlifting configurations.

FINITE-DIFFERENCE APPROXIMATIONS

Governing Equation

The approximate equation and boundary conditions for transonic flow over slender body, thin wing configurations, such as shown in figure 1, are derived from transonic small disturbance theory under the assumptions of small flow deflections and a free-stream Mach number near unity. The governing equation is

$$\left[(1 - M_\infty^2)\ \phi_x - \frac{\gamma + 1}{2} M_\infty^n\ \phi_x^2\right]_x + \left[\phi_y\right]_y + \left[\phi_z\right]_z = 0 \qquad (1)$$

where ϕ is the disturbance velocity potential, M_∞ is the free-stream Mach number, and γ is the ratio of specific heats. The parameter n reflects the nonuniqueness of equation (1), and it can be adjusted to better approximate the exact sonic pressure coefficient. For example, see reference 14.

Murman (ref. 15) has shown that the shock jump relation implied by equation (1) is contained in the difference approximations if they are written in conservation form. That is, mass fluxes at cell boundaries interior to the computation mesh cancel identically. The present conservative finite difference equation is derived by applying the divergence theorem to the integral of equation (1)(the transonic approximation to mass conservation) over an elemental, rectangular, computation volume or cell as shown in figure 2. Define the mass flux as

$$\begin{aligned}\vec{F} &= f\,\vec{i}_x + g\,\vec{i}_y + h\,\vec{i}_z \\ &= \left[(1 - M_\infty^2)\ \phi_x - \frac{\gamma + 1}{2} M_\infty^n\ \phi_x^2\right]\vec{i}_x + \left[\phi_y\right]\vec{i}_y + \left[\phi_z\right]\vec{i}_z \end{aligned} \qquad (2)$$

Applying the divergence theorem to the volume integral and dividing by the cell volume results in the difference expression

$$\frac{f_{i+1/2,j,k} - f_{i-1/2,j,k}}{x_{i+1/2} - x_{i-1/2}} + \frac{g_{i,j+1/2,k} - g_{i,j-1/2,k}}{y_{j+1/2} - y_{j-1/2}} + \frac{h_{i,j,k+1/2} - h_{i,j,k-1/2}}{z_{k+1/2} - z_{k-1/2}} = 0 \tag{3}$$

for the point (x_i, y_j, z_k). If the velocities are defined by

$$(\phi_x)_{i+1/2,j,k} = \frac{\phi_{i+1,j,k} - \phi_{i,j,k}}{x_{i+1} - x_i}$$

$$(\phi_y)_{i,j+1/2,k} = \frac{\phi_{i,j+1,k} - \phi_{i,j,k}}{y_{j+1} - y_j}, \text{ etc.}$$

the finite difference approximations to the fluxes are

$$\left.\begin{aligned} f_{i+1/2,j,k} &= (1 - \mu_{i,j,k})\left[(1 - M_\infty^2)\,\phi_x - \frac{\gamma + 1}{2} M_\infty^n \phi_x^2\right]_{i+1/2,j,k} \\ &\quad + \mu_{i,j,k}\left[(1 - M_\infty^2)\,\phi_x - \frac{\gamma + 1}{2} M_\infty^n \phi_x^2\right]_{i-1/2,j,k} \\ f_{i-1/2,j,k} &= (1 - \mu_{i-1,j,k})\left[(1 - M_\infty^2)\,\phi_x - \frac{\gamma + 1}{2} M_\infty^n \phi_x^2\right]_{i-1/2,j,k} \\ &\quad + \mu_{i-1,j,k}\left[(1 - M_\infty^2)\,\phi_x - \frac{\gamma + 1}{2} M_\infty^n \phi_x^2\right]_{i-3/2,j,k} \end{aligned}\right\} \tag{4}$$

$$g_{i,j+1/2,k} = [\phi_y]_{i,j+1/2,k}, \quad g_{i,j-1/2,k} = [\phi_y]_{i,j-1/2,k} \tag{5}$$

$$h_{i,j,k+1/2} = [\phi_z]_{i,j,k+1/2}, \quad h_{i,j,k-1/2} = [\phi_z]_{i,j,k-1/2} \tag{6}$$

which, when substituted into equation (3) and factored, give the final difference approximation

$$\Big\{(1-\mu_{i,j,k})(1-M^2)_{i,j,k}\left[(\phi_x)_{i+1/2,j,k}-(\phi_x)_{i-1/2,j,k}\right]$$

$$+\mu_{i-1,j,k}(1-M^2)_{i-1,j,k}\left[(\phi_x)_{i-1/2,j,k}-(\phi_x)_{i-3/2,j,k}\right]\Big\}\Big/(x_{i+1/2}-x_{i-1/2})$$

$$+\left[(\phi_y)_{i,j+1/2,k}-(\phi_y)_{i,j-1/2,k}\right]\Big/(y_{j+1/2}-y_{j-1/2})$$

$$+\left[(\phi_z)_{i,j,k+1/2}-(\phi_z)_{i,j,k-1/2}\right]\Big/(z_{k+1/2}-z_{k-1/2})=0 \qquad (7)$$

where

$$(1-M^2)_{i,j,k}=1-M_\infty^2-(\gamma+1)M_\infty^n\frac{1}{2}\left[(\phi_x)_{i+1/2,j,k}+(\phi_x)_{i-1/2,j,k}\right] \qquad (8)$$

$$\mu_{i,j,k}=\begin{cases}0 \text{ for } (1-M^2)_{i,j,k}>0\\ 1 \text{ for } (1-M^2)_{i,j,k}<0\end{cases} \qquad (9)$$

The switching parameter $\mu_{i,j,k}$ gives the flux in the x-direction by a central difference operator in elliptic regions ($\mu_{i-1,j,k}=0$, $\mu_{i,j,k}=0$) and by a central operator shifted upstream one mesh point in hyperbolic regions ($\mu_{i-1,j,k}=1$, $\mu_{i,j,k}=1$) and thereby prevents upstream signal propagation. For evenly spaced meshes equation (7) is formally second order accurate in elliptic regions and first order in hyperbolic regions.

In addition to the elliptic and hyperbolic operators, equation (7) also contains the parabolic ($\mu_{i-1,j,k}=0$, $\mu_{i,j,k}=1$) and shock point ($\mu_{i-1,j,k}=1$, $\mu_{i,j,k}=0$) operators and, for evenly spaced meshes, is the three-dimensional equivalent of Murman's fully conservative relaxation (FCR) method (ref. 15). In the unequally spaced mesh case (both two and three dimensions), however, the first term of equation (7) differs by a factor of $\frac{x_i-x_{i-2}}{x_{i+1}-x_{i-1}}$ in hyperbolic regions because the mesh cells are centered about the point (i,j,k) in all flow regions. Consistency of the difference approximation is demonstrated for smoothly varying meshes by the expansion

$$\frac{x_i-x_{i-2}}{x_{i+1}-x_{i-1}}=1-\Delta\xi\,\frac{\xi''}{\xi'}+0(\Delta\xi^2) \qquad (10)$$

where $\xi(x)$ is the inverse of the implied stretching function, that is, $\Delta\xi$ is uniform, and the primes denote derivatives.

A majority of 2-D transonic calculations and all reported 3-D calculations have been performed by use of nonconservative relaxation (NCR) methods. In the absence of viscosity corrections, the NCR solutions generally agree

better with experimental pressure measurements than the FCR results. This is because mass sources result from the failure of the NCR methods to cancel fluxes at shock points, where x-differences shift from upwind to centered (ref. 15). The source strengths do not vanish with vanishing mesh spacing, and they reduce the computed shock strengths to values nearly equal to those obtained experimentally, which are, of course, weakened by the interaction of the shock and boundary layer.

Two NCR methods are contained in equation (7). The first, that due to Murman and Cole (ref. 1), is obtained by setting

$$\mu_{i-1,j,k} = \mu_{i,j,k} \tag{11}$$

except at the expansion sonic line, and the second, that due to Garabedian and Korn (ref. 16), is obtained by setting

$$\left[(1 - M_\infty^2)\mu\right]_{i-1,j,k} = \left[(1 - M_\infty^2)\mu\right]_{i,j,k} \tag{12}$$

Wing Boundary Conditions

For a wing whose surface is given by $f(x,y,z) = 0$ and which is at angle of attack α, the linearized boundary condition is

$$f_x + (\phi_z + \alpha) f_z = 0 \tag{13}$$

This equation is applied on the wing mean plane midway between mesh planes by expressing the vertical derivative at the mesh plane adjacent to the upper surface as

$$\left(\phi_{zz}\right)_{i,j,k} = \frac{2}{z_{k+1} - z_{k-1}} \left\{ \frac{\phi_{i,j,k+1} - \phi_{i,j,k}}{z_{k+1} - z_k} + \left[\left(\frac{f_x}{f_z} \right)_u + \alpha \right] \right\} \tag{14a}$$

and the lower surface as

$$\left(\phi_{zz}\right)_{i,j,k} = \frac{-2}{z_{k+1} - z_{k-1}} \left\{ \frac{\phi_{i,j,k} - \phi_{i,j,k-1}}{z_k - z_{k-1}} + \left[\left(\frac{f_x}{f_z} \right)_\ell + \alpha \right] \right\} \tag{14b}$$

The Kutta condition requires that the pressure (ϕ_x) be continuous at the trailing edge. This fixes the section circulation Γ_j, which is equal to the difference in potential at the section trailing edge linearly extrapolated from points above and below. The potential jumps are convected downstream along straight lines to form the trailing-vortex sheet, across which both pressure and downwash (ϕ_z) are continuous. The potential jump through the sheet is taken into account in the ϕ_{zz} difference formula at the plane above by replacing $\phi_{i,j,k-1}$ with $\phi_{i,j,k-1} + \Gamma_j$ and at the plane below by replacing $\phi_{i,j,k+1}$ with $\phi_{i,j,k+1} - \Gamma_j$. Note that no points lie on the sheet, as in the original method (ref. 2). The present technique simplifies the coding with no significant loss in accuracy.

Fuselage Boundary Condition

In the present method the fuselage is treated in a rectangular mesh system. A similar two-dimensional procedure, which appears to be extendable to three dimensions, has been demonstrated for subsonic flow in reference 17. In the present method a simplified approach suggested by Allen Chen of the Boeing Co. is used in which the mesh is constructed so that points lie reasonably close to the fuselage surface, such as shown in figure 3. Points may lie either inside or outside the fuselage boundary. For a configuration described by $f(x,y,z) = 0$, the small-disturbance boundary condition becomes

$$f_x + \phi_y f_y + \phi_z f_z = 0 \tag{15}$$

By substituting three point-extrapolated differences at the boundary point i,j,k (for the upper surface, say) of the form

$$\left(\phi_y\right)_{i,j,k} = A_1\,\phi_{i,j,k} + A_2\,\phi_{i,j-1,k} + A_3\,\phi_{i,j-2,k} \tag{16a}$$

and

$$\left(\phi_z\right)_{i,j,k} = B_1\,\phi_{i,j,k} + B_2\,\phi_{i,j,k-1} + B_3\,\phi_{i,j,k-2} \tag{16b}$$

into equation (15), the expression for the boundary potential is found as

$$\phi_{i,j,k} = -\left[f_x + (A_2\,\phi_{i,j-1,k} + A_3\,\phi_{i,j-2,k})f_y + (B_2\,\phi_{i,j,k-1} + B_3\,\phi_{i,j,k-2})f_z\right] \Big/ (A_1 f_y + B_1 f_z) \tag{17}$$

Far Field

The condition applied at the outer boundary of the computational domain is given by the superposition of the asymptotic far-field solutions for wings derived by Klunker (ref. 18), and bodies of revolution derived by Krupp and Murman (ref. 19). At the downstream boundary, however, the lift contribution is obtained by the numerical solution to the cross-flow equation.

Nonrectangular Wing Transformation

The isolated wing code treats a swept and tapered wing by mapping the wing into a rectangle by the transformation

$$\left.\begin{aligned} \xi &= \frac{x - x_{LE}}{x_{TE} - x_{LE}} \\ \eta &= y \\ \zeta &= z \end{aligned}\right\} \tag{18}$$

where x_{LE} and x_{TE} are the x-coordinates of the leading and trailing edges. The divergence form of equation (1) becomes

$$\left[(1 - M_\infty^2)\xi_x\phi_\xi - \frac{\gamma + 1}{2} M_\infty^n \xi_x^2 \phi_\xi^2 + \frac{\xi_y}{\xi_x}(\xi_y\phi_\xi + \phi_\eta)\right]_\xi + \left[\frac{1}{\xi_x}(\xi_y\phi_\xi + \phi_\eta)\right]_\eta + \left[\frac{1}{\xi_x}\phi_\zeta\right]_\zeta \tag{19}$$

The conservative difference approximation of equation (19) is derived in the manner previously outlined and is given as

$$\begin{aligned}
&\Bigg\{ (1 - \mu_{i,j,k})(1 - M^2)_{i,j,k} \left[(\xi_x\phi_\xi)_{i+1/2,j,k} - (\xi_x\phi_\xi)_{i-1/2,j,k}\right] \\
&+ \mu_{i-1,j,k}\,(1 - M^2)_{i-1,j,k} \left[(\xi_x\phi_\xi)_{i-1/2,j,k} - (\xi_x\phi_\xi)_{i-3/2,j,k}\right] \\
&+ \left[\frac{\xi_y}{\xi_x}(\xi_y\phi_\xi + \phi_\eta)\right]_{i+1/2,j,k} - \left[\frac{\xi_y}{\xi_x}(\xi_y\phi_\xi + \phi_\eta)\right]_{i-1/2,j,k} \Bigg\} \Big/ (\xi_{i+1/2} - \xi_{i-1/2}) \\
&+ \left\{ \left[\frac{1}{\xi_x}(\xi_y\phi_\xi + \phi_\eta)\right]_{i,j+1/2,k} - \left[\frac{1}{\xi_x}(\xi_y\phi_\xi + \phi_\eta)\right]_{i,j-1/2,k} \right\} \Big/ (\eta_{j+1/2} - \eta_{j-1/2}) \\
&+ \left[\left(\frac{1}{\xi_x}\phi_\zeta\right)_{i,j,k+1/2} - \left(\frac{1}{\xi_x}\phi_\zeta\right)_{i,j,k-1/2}\right] \Big/ (\zeta_{k+1/2} - \zeta_{k-1/2}) = 0
\end{aligned} \tag{20}$$

where

$$(\phi_\xi)_{i+1/2,j,k} = \frac{\phi_{i+1,j,k} - \phi_{i,j,k}}{\xi_{i+1} - \xi_i}$$

$$(\phi_\eta)_{i+1/2,j,k} = \frac{1}{2}\left[\frac{\phi_{i+1,j+1,k} - \phi_{i+1,j-1,k}}{\eta_{j+1} - \eta_{j-1}} + \frac{\phi_{i,j+1,k} - \phi_{i,j-1,k}}{\eta_{j+1} - \eta_{j-1}}\right], \text{ etc.}$$

Note that equation (20) maintains the proper domain of dependence in hyperbolic regions by upwind differencing only the contribution from the x-direction (i.e., terms multiplied by $(1 - \mu_{i,j,k})$ and $\mu_{i-1,j,k}$) while the others remain centrally differenced.

In transformed coordinates the wing surface and vortex sheet conditions are unaltered. However, the boundary condition at the wing root becomes

$$\phi_y = \xi_y \phi_\xi + \phi_\eta = 0 \tag{21}$$

and is substituted into equation (20) at the root.

Relaxation Scheme

The solution of the difference equations is obtained by a vertical-column relaxation scheme. A number of variations of the method have been coded, and in what follows, we outline the scheme that we believe has the best stability properties.

Following Jameson (ref. 20), the iterations are viewed as steps in pseudo-time. The combination of new (ϕ^+) and old (ϕ) values in the difference operators is chosen so that the related time-dependent equation represents a properly posed problem whose steady-state solution approaches that of the steady equation. In addition, the linearized algorithm is required to satisfy the von Neumann stability criterion.

For ease of discussion, consider an evenly spaced rectangular mesh with $x_{i+1} = x_i + \Delta x$, etc. The relaxation equation for elliptic regions ($\mu_{i,j,k} = 0$ and $\mu_{i-1,j,k} = 0$) is written

$$(1 - M^2)_{i,j,k} \left[\phi^+_{i-1,j,k} - \frac{2}{\omega}\phi^+_{i,j,k} - 2\left(1 - \frac{1}{\omega}\right)\phi_{i,j,k} + \phi_{i+1,j,k}\right] \Big/ (\Delta x)^2$$

$$+ \left[\phi^+_{i,j-1,k} - 2\phi^+_{i,j,k} + \phi_{i,j+1,k}\right] \Big/ (\Delta y)^2$$

$$+ \left[\phi^+_{i,j,k-1} - 2\phi^+_{i,j,k} + \phi^+_{i,j,k+1}\right] \Big/ (\Delta z)^2 = 0 \tag{22}$$

where ω is an overrelaxation parameter ($1 \leqslant \omega < 2$) and $M_{i,j,k}$ is evaluated from old values. Note that only the contribution from the x-direction is overrelaxed. This avoids an abrupt change in the diagonal term as the solution crosses the sonic surface suggested by J. C. South and P. A. Newman of the Langley Research Center.

In hyperbolic regions the relaxation equation is

$$(1 - M^2)_{i-1,j,k} \left(\phi_{i-2,j,k} - 2\phi^+_{i-1,j,k} + 2\phi^+_{i,j,k} - \phi_{i,j,k}\right) / (\Delta x)^2$$

$$+ \left(\phi^+_{i,j-1,k} - \phi^+_{i,j,k} - \phi_{i,j,k} + \phi_{i,j+1,k}\right) / (\Delta y)^2$$

$$+ \left(\phi^+_{i,j,k-1} - 2\phi^+_{i,j,k} + \phi^+_{i,j,k+1}\right) / (\Delta z)^2 = 0 \tag{23}$$

It is of interest to look at the equivalent time-dependent equation

$$(M^2 - 1)\phi_{xx} - \phi_{yy} - \phi_{zz} + 2(M^2 - 1)\frac{\Delta t}{\Delta x}\phi_{xt} + \frac{\Delta t}{\Delta y}\phi_{yt} = 0 \tag{24}$$

inferred from equation (23). It can be shown that the condition

$$(M^2 - 1)\frac{\Delta t}{\Delta x} > \frac{(M^2 - 1)^{1/2}}{2}\frac{\Delta t}{\Delta y} \tag{25}$$

must hold for x to be the hyperbolic marching direction. To keep x the marching direction and to improve stability near sonic points, it may be necessary to add to equation (23) the quantity

$$\epsilon(M^2 - 1)^{1/2}\frac{\Delta t}{\Delta x}\phi_{xt} \tag{26}$$

where

$$\frac{\Delta t}{\Delta x}\phi_{xt} = (\phi^{+}_{i,j,k} - \phi_{i,j,k} - \phi^{+}_{i-1,j,k} + \phi_{i-1,j,k})/(\Delta x)^2$$

and ϵ is a chosen parameter.

RESULTS

In this section we discuss comparisons between present computed results, other theoretical solutions, and experimental data. Before beginning, however, we wish to point out the difficulties associated with comparing computed solutions with experiment. It is well known that viscous effects play a large role in determining surface pressure distributions in many transonic flows. This is particularly true in lifting cases (ref. 21) and when embedded shock waves occur. (See ref. 13, fig. 6.) Since the present method is entirely inviscid, considerable disagreement with data is encountered where viscous effects are significant. Furthermore, wind-tunnel results are often affected by interference from the tunnel walls. Although attempts are made to correct for interference effects, the corrected free-stream Mach number and angle of attack do not always closely correspond to free-air values. Also, as the free-stream Mach number approaches one, the wall effects on the sonic bubble and shock locations become even more significant and difficult to assess.

Violation of the small-disturbance assumption can also cause significant departures from the correct inviscid free-air solution. The assumption of small flow deflection is seriously violated near blunt leading edges and at high angles of attack. Thus, erroneous results can be obtained in the leading-edge region. Also, the small-disturbance theory predicts shock pressure jumps that become significantly stronger than the Rankine-Hugoniot value as the shock Mach number increases past about 1.3. Finally, the predictions for oblique shock waves also depart significantly from the exact values for shock wave angles in excess of about 20° (ref. 13).

We begin by considering comparisons for two isolated wings. The first, shown in figure 4, is for computed and experimental pressures furnished by M. G. Hall of the RAE on the RAE Wing C at $M = 0.95$ and $\alpha = 0^{\circ}$ which was tested in the RAE 8 ft x 6 ft transonic tunnel at $Re_c = 1.4 \times 10^6$. The computed results, which were obtained on a $51 \times 34 \times 48$ (x,y,z) grid, show generally good agreement with the experimental pressures, with some overexpansion near the leading edge at the root. The NCR and FCR solutions were virtually the same because of the absence of shock waves.

The second comparison, in figures 5 and 6, is for the ONERA M6 wing. The experimental data were obtained in the ONERA S2 transonic tunnel at $Re_c \approx 2.5 \times 10^6$ (ref. 22). Computations were performed on a sequence of three grids ($35 \times 20 \times 24$, $45 \times 23 \times 30$, $66 \times 37 \times 32$), using both the NCR and FCR methods, and required approximately 5 CPU minutes on the CDC 7600 computer utilizing the RUN 76 compiler. Figure 5 shows comparisons between the computed and measured pressures for $M = .84$ and $\alpha = 3^{\circ}$. The NCR results are very similar to those reported in reference 5. The FCR method predicts a slightly downstream shift in shock location, as expected from Murman's two-dimensional computations (ref. 15). Although the experimental pressures show evidence of both a forward and an aft shock wave, the calculations show clear evidence of only the aft shock. This is not surprising, because it has been shown in reference 13 that the small-disturbance equation (used here and in ref. 5) is a poor approximation to the full potential equation for shocks with sweep angles greater than about 20°. The experimental forward shock is swept at about 36° over most of its length. The agreement claimed in reference 5 between computed and experimental forward shock locations is not evident in the comparison of experimental and computed section pressures. It appears that the small-disturbance approach can, however, be modified to properly treat swept shock waves by retaining two additional terms in the governing equation. (See ref. 13.) Work in this area is currently being pursued.

Figure 6 shows pressure comparisons for $M = .92$ and $\alpha = 3^{\circ}$. Here the aft shock prediction from the FCR method is significantly downstream of that predicted by the NCR method. The NCR result, with the weaker shock, generally agrees better with the data but is still in serious disagreement. Neither method captures the forward shock, which is clearly evident in the experimental data at the three outboard span stations. The disagreement in upper surface, aft shock, and lower surface shock locations can probably be attributed primarily to the decrease in wing lift caused by trailing-edge viscous effects. This moves the upper shock upstream and the lower one downstream.

We now turn our attention to comparisons of computed and experimental pressures for a parabolic-arc body with sting, shown in figure 7, and wing-fuselage configurations, shown in figures 8 to 10. The present results are obtained by use of equation (17) as the body boundary condition. Figure 7 shows pressures at the body surface and in the flow field at two body diameters from the centerline for $M_\infty = .99$. Good agreement is shown between the present NCR calculation ($41 \times 40 \times 40$), an axisymmetric NCR calculation (ref. 23), and measured pressures (ref. 24). The x-mesh spacing used in the present calculation is 2.5 times coarser than that used in the axisymmetric

one, and accounts for the difference in shock resolution. The discrepancies in the pressures are primarily attributed to the mesh coarseness and the lack of boundary definition near the body nose. Figure 8 compares NCR, FCR, linear theory (ref. 25), and experimental pressures (ref. 25) for a Sears-Haack fuselage rectangular-wing combination at $M_\infty = .90$ and $\alpha = 0°$. The data were obtained in the AEDC 16 ft wind tunnel at $Re_{\bar{c}} = 3.0 \times 10^6$ (ref. 26). The present results were obtained on a $57 \times 35 \times 30$ grid. The pressure plots at the top of the body show that the present results overexpand near the nose compared with linear theory, as was noted in the previous example. As usual, the FCR-predicted shock location is aft of the NCR prediction, whereas linear theory shows no shock. Comparison with experiment is good although the sparseness of the data points precludes the accurate determination of the experimental shock location. A comparison is also shown at mid semispan. The interesting result here is that the experimental shock location is downstream of the computed locations. In figure 9 the mid-semispan solution is compared with an isolated wing calculation (ref. 25) from the Jameson 3-D program and data. The present results and those of Jameson compare favorably, particularly when the coarseness of the mesh used in the present calculation is considered. The disagreement between the computations and experiment does not appear to be caused by viscous effects, which generally move shocks upstream in such nonlifting cases. More likely the disagreement is caused by the test Mach number being slightly higher than .90.

Finally, figure 10 compares NCR calculated and experimental pressures for a swept wing-fuselage configuration at $M = .93$ and $\alpha = 0°$. The computed results were obtained using a Cartesian grid ($81 \times 59 \times 27$) for the wing as well as the fuselage. The first x-mesh point at the wing leading edge was fixed at 2.5 percent chord with 23 mesh points along the root chord and 11 along the tip chord, distributed according to the methods used in references 3 and 5. The uncorrected experimental data were obtained in the Langley 8-ft tunnel (solid wall) at $Re_{\bar{c}} = 2.0 \times 10^6$ (ref. 27). The agreement with experiment on the fuselage centerline and the two inboard panels is good. In the computed results, the wing root shock propagates laterally to $y/b = .60$, but the experimental shock dissipates before reaching this point. The source of the disagreement is not clear but perhaps is a viscous effect.

Clearly, the computed results lack sufficient leading-edge expansion at the outboard span stations $y/b = .80$ and $y/b = .95$, an effect that is caused by the coarse x mesh (about 12 points per chord) there. The Cartesian grid approach requires too many mesh points to obtain the required resolution near the leading edge. The calculation should be improved significantly by the use of the planform transformation, which was described previously in the treatment of isolated wings.

CONCLUDING REMARKS

A relaxation method has been developed which allows as an option either fully conservative (FCR) or nonconservative (NCR) differencing. The three-dimensional FCR and NCR solutions exhibit properties similar to those

reported by Murman for two-dimensional flow. That is, for weak shock waves there is little difference; as the shock strength increases, the FCR shock wave becomes stronger than the NCR shock wave and, consequently, is located further downstream. The NCR solutions correlate better with experimental pressures, but it is anticipated that the FCR method will prove superior when viscous effects are properly accounted for.

Clearly, the present solutions do not agree well with data in all cases, particularly when (1) there is extensive separation either at the shock or trailing edge, and when (2) there are highly swept shock waves embedded in the flow. The treatment of highly swept shocks should be improved by retaining two additional terms in the governing equation, as suggested in reference 13, or by solution of the full potential equations.

In flows about wing-fuselage configurations, the basic idea is to treat the fuselage with accuracy sufficient to obtain its effect on the wing without the use of complicated fuselage transformations. The present results are encouraging and felt to be quite good when the simple boundary approximations used are considered. The extension to lifting wing-fuselage configurations is straightforward and work in this area is being pursued.

REFERENCES

1. Murman, E. M., and Cole, J. D.: Calculation of Plane Steady Transonic AIAA Journal, vol. 9, no. 1, January 1971, pp. 114-121.

2. Ballhaus, W. F., and Bailey, F. R.: Numerical Calculation of Transonic Flow About Swept Wings. AIAA Paper 72-677, June 1972.

3. Bailey, F. R., and Ballhaus, W. F.: Relaxation Methods for Transonic Flow About Wing-Cylinder Combinations and Lifting Swept Wings. Lecture Notes in Physics, vol. 19, Springer-Verlag, 1972, pp. 2-9.

4. Bailey, F. R.: On the Computation of Two- and Three-Dimensional Steady Transonic Flows by Relaxation Methods. VKI Lecture Series "Progress in Numerical Fluid Dynamics," Von Karman Institute for Fluid Dynamics, Rhode-St-Genese, Belgium, February 11-15, 1974.

5. Schmidt, W., Rohlfs, S., and Vanino, R.: Some Results Using Relaxation Methods and Finite Volume Techniques for Two- and Three-Dimensional Transonic Flows. Lecture Notes in Physics, vol. 35, Springer-Verlag, 1974, pp. 364-372.

6. Klunker, E. B., and Newman, P. A.: Computation of Transonic Flow About Lifting Wing-Cylinder Combinations. Jour. Aircraft, vol. 2, no. 4, April 1974, pp. 254-256.

7. Newman, P. A., and Klunker, E. B.: Computation of Transonic Flow About Finite Lifting Wings. AIAA Journal, vol, 10, no. 7, July 1972, pp. 971-973.

8. Bailey, F. R., and Steger, J. L.: Relaxation Techniques for Three Dimensional Transonic Flow About Wings. AIAA Paper 72-189, Jan. 1972.

9. Ballhaus, W. F., and Caradonna, F. X.: The Effect of Planform Shape on the Transonic Flow Past Rotor Tips. Aerodynamics of Rotary Wings, AGARD Conference Proceedings No. 111, Paper 17, Sept. 1972.

10. Isom, M. P., and Caradonna, F. X.: Subsonic and Transonic Potential Flow Over Helicopter Rotor Blades. AIAA Paper 72-39, Jan. 1972.

11. Jameson, A.: Numerical Calculation of the Three Dimensional Transonic Flow Over a Yawed Wing. Proceedings AIAA Computational Fluid Dynamics Conference, Palm Springs, CA, July 1973, pp. 18-26.

12. Lores, M. E., and Lemmerman, L. A.: A Numerical Method for Isolated Wing Transonic Flow Calculations. LTV Tech. Rept. no. 2-57110/4R-3190, Nov. 1974.

13. Lomax, H., Bailey, F. R., and Ballhaus, W. F.: On the Numerical Simulation of Three-Dimensional Transonic Flow With Application to the C-141 Wing. NASA TN D-6933, 1973.

14. Krupp, J. A.: The Numerical Calculation of Plane Steady Transonic Flows Past Thin Lifting Airfoils. Boeing Scientific Research Laboratories Report D180-12958-1, June 1971.

15. Murman, E. M.: Analysis of Embedded Shock Waves Calculated by Relaxation Methods. Proceedings of AIAA Computational Fluid Dynamics Conference, Palm Springs, CA, July 1973, pp. 27-40.

16. Garabedian, P. R., and Korn, D. G.: Analysis of Transonic Airfoils. Comm. Pure Appl. Math., vol. XXIV, 1971, pp. 841-851.

17. Parker, R., and Ma, C. Y.: Normal Gradient Boundary Condition in Finite Difference Calculations. Intl. Jour. Num. Meth. Eng., vol. 7, 1973, pp. 395-411.

18. Klunker, E. B.: Contributions to Methods for Calculating the Flow About Thin Lifting Wings at Transonic Speeds — Analytical Expression for the Far Field. NASA TN D-6530, 1971.

19. Krupp, J. A., and Murman, E. M.: The Numerical Calculation of Steady Transonic Flows Past Thin Lifting Airfoils and Slender Bodies. AIAA Paper 71-566, June 1971.

20. Jameson, Antony: Iterative Solution of Transonic Flows over Airfoils and Wings, Including Flows at Mach 1. Comm. Pure Appl. Math., vol. XXVII, 1974, pp. 283-309.

21. Melnik, R. E., and Ives, D. C.: On Viscous and Wind-Tunnel Wall Effects in Transonic Flows Over Airfoils. AIAA Paper 73-660, July 1973.

22. Monnerie, B., and Charpin, F.: Essais de Buffeting d'une Aile en Fleche en Transsonique. 10e Colloque D'Aérodynamique Appliquée, Nov. 1973.

23. Bailey, F. R.: Numerical Calculation of Transonic Flow About Slender Bodies of Revolution. NASA TN D-6582, 1971.

24. Taylor, R. A., and McDevitt, J. B.: Pressure Distributions at Transonic Speeds for Parabolic-Arc Bodies of Revolution Having Fineness Ratios of 10, 12, and 14. NACA TN 4234, 1958.

25. Newman, P. A., and Allison, D. O.: Comparison of Interference-Free Numerical Results with Sample Experimental Data for the AEDC Wall-Interference Model at Transonic and Subsonic Flow Conditions. NASA TM X-71991, 1974.

26. Binion, T. W.: An Investigation of Three Dimensional Wall Interference in a Variable Porosity Transonic Wind Tunnel. AEDC-TR-74-76, 1973.

27. Loving, D. L., and Estabrooks, B. B.: Transonic-Wing Investigation in the Langley 8-Foot High-Speed Tunnel at High Subsonic Mach Numbers and at a Mach Number of 1.2. NACA RM L51F07, 1951.

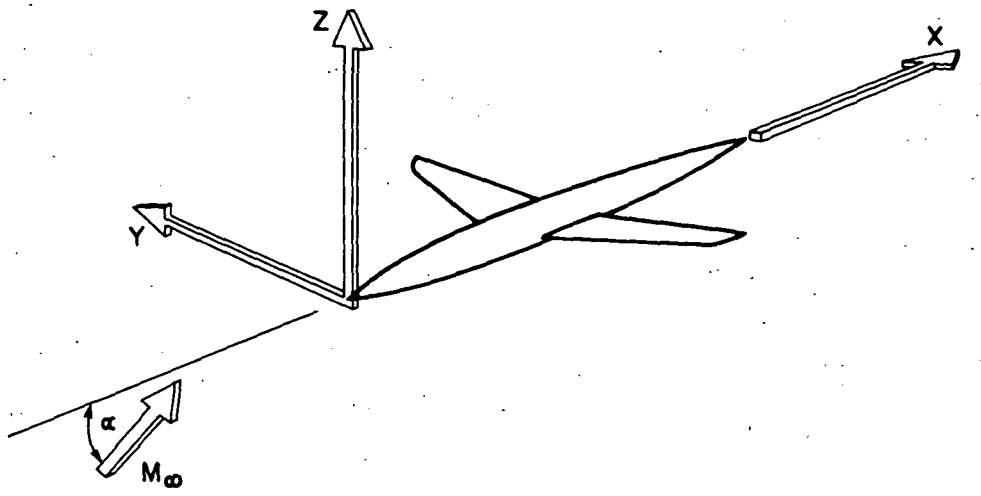

Figure 1.— Coordinate system.

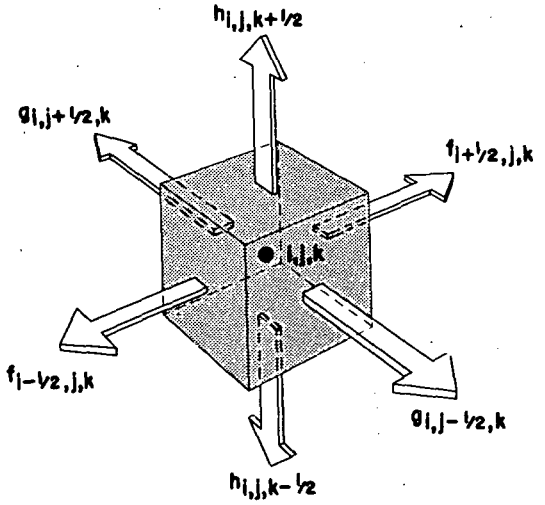

Figure 2.— Computational volume.

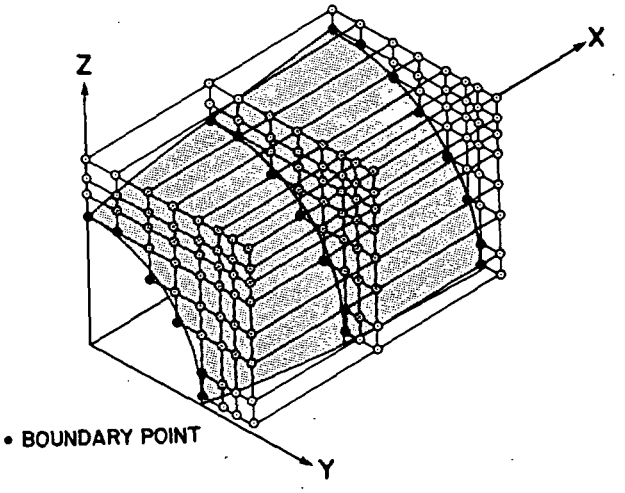

Figure 3.— Body boundary points.

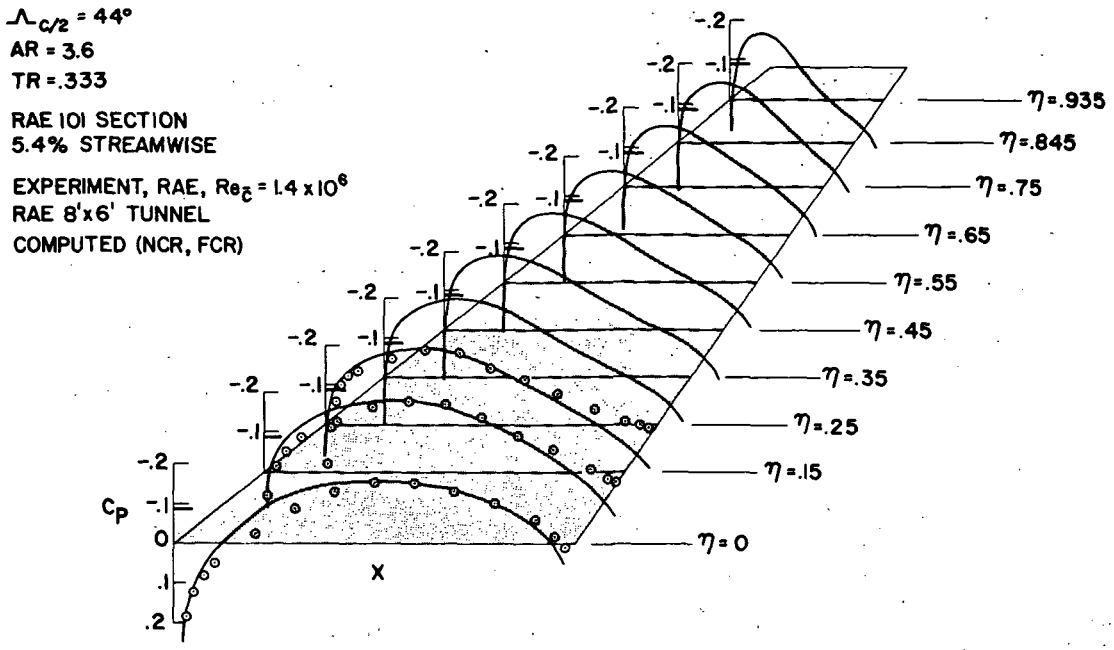

Figure 4.- Comparison of computed and experimental pressure coefficients C_P for the RAE wing C. $M_\infty = 0.95$; $\alpha = 0^o$; TR denotes taper ratio; and AR denotes aspect ratio.

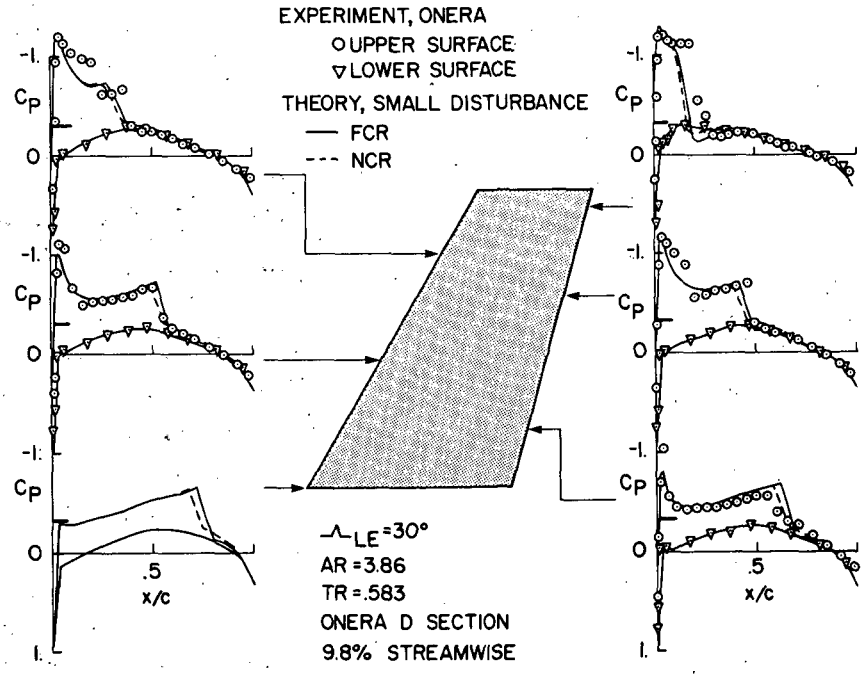

Figure 5.- Comparison of computed and experimental (ref. 22) pressure coefficients C_P for the ONERA M6 wing. $M_\infty = 0.84$; $\alpha = 3^o$.

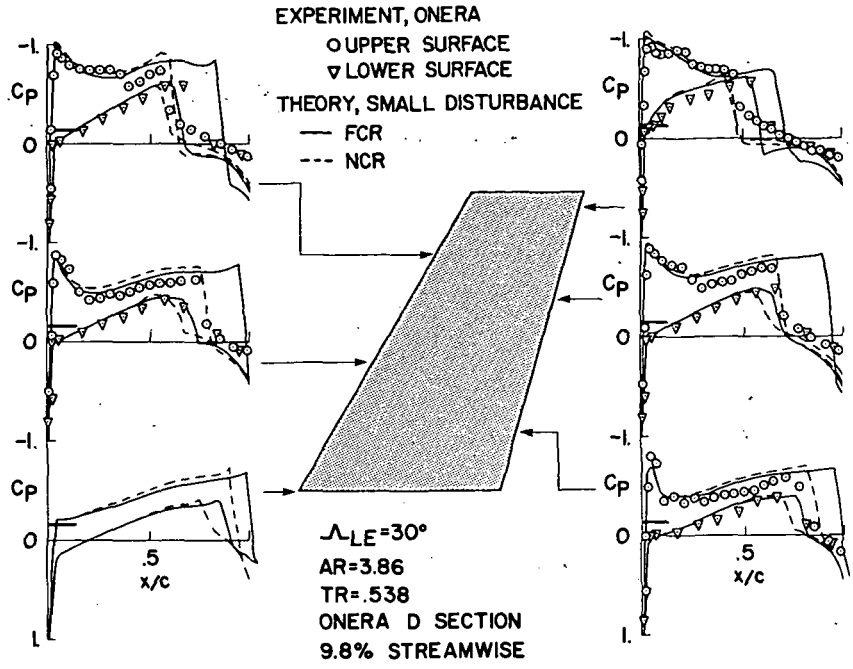

Figure 6.- Comparison of computed and experimental (ref. 22) pressure coefficients C_p for the ONERA M6 wing, $M_\infty = 0.92$; $\alpha = 3^\circ$.

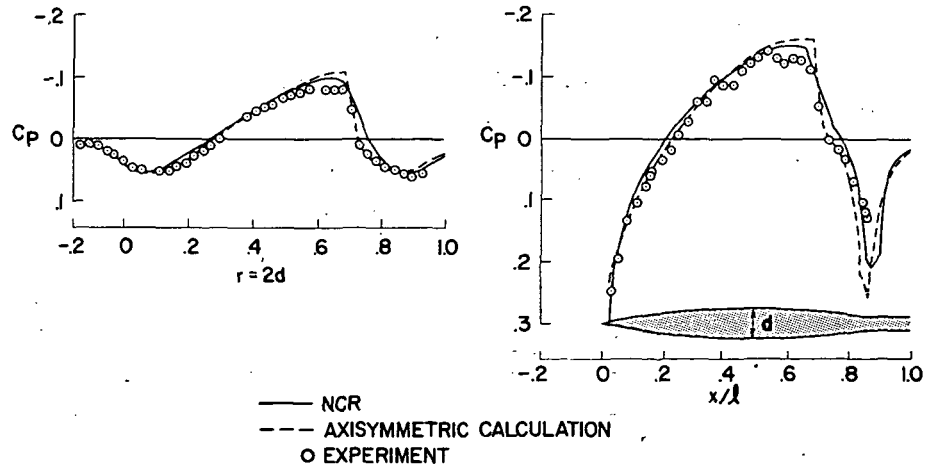

Figure 7.- Comparison with computed (ref. 23) and experimental (ref. 24) pressure coefficients C_p for a parabolic arc of revolution. Fineness ratio, 10; $M_\infty = 0.99$.

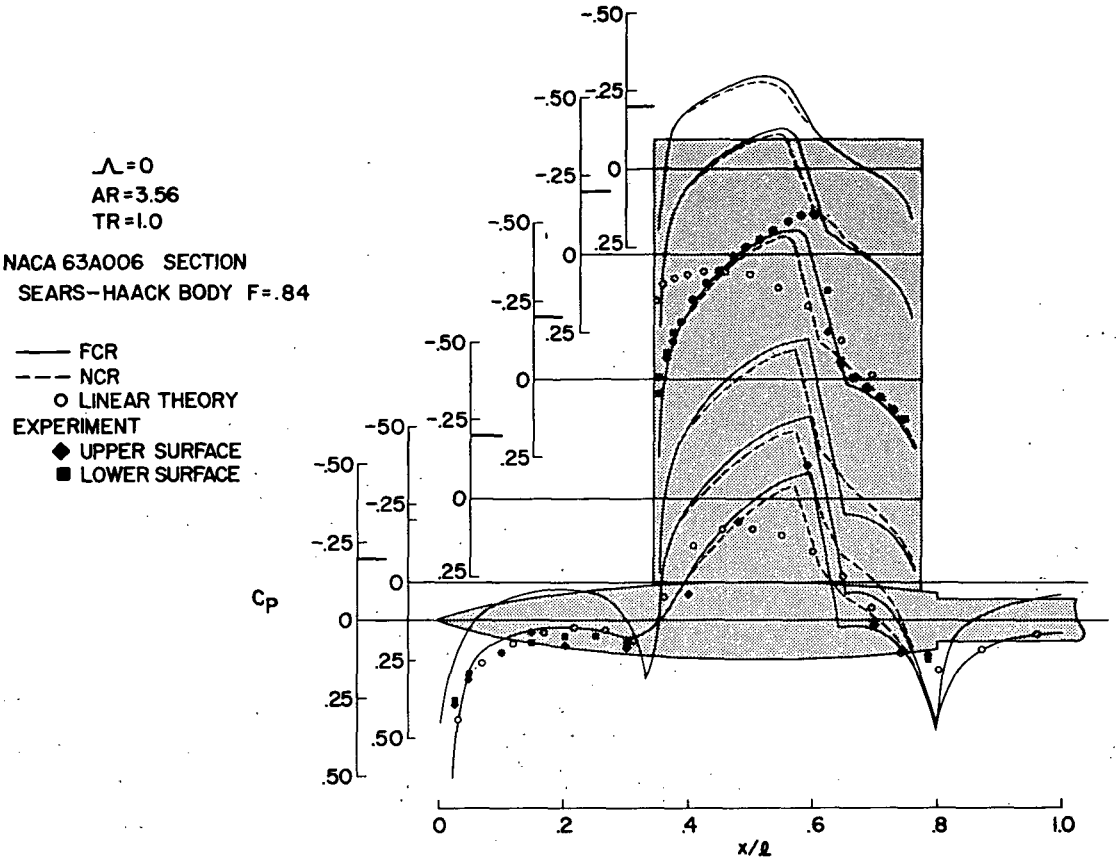

Figure 8.- Comparison with computed (ref. 25) and experimental (ref. 26) pressure coefficients C_p for a rectangular-wing—fuselage configuration. $M_\infty = 0.90$; $\alpha = 0^o$.

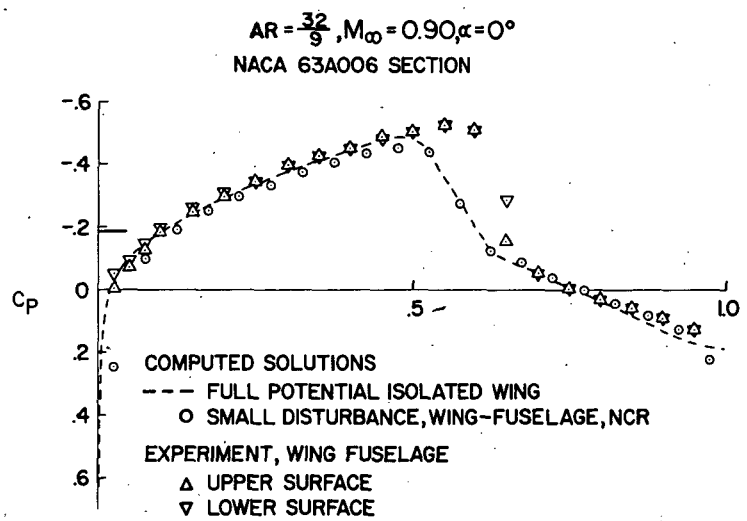

Figure 9.- Comparison of computed small disturbance and full potential (ref. 25) pressure coefficients Cp with experiment (ref. 26) at mid-semispan location.

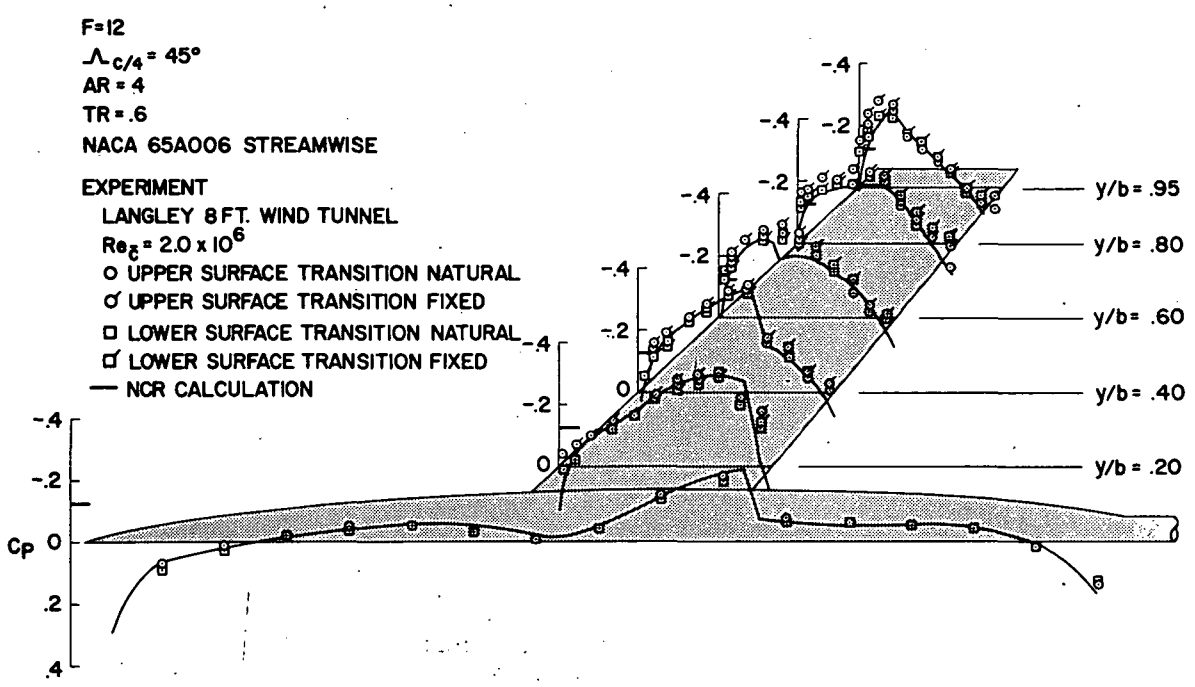

Figure 10.- Comparison of computed and experimental (ref. 27) pressure coefficients C_p for swept-wing—fuselage configuration. $M_\infty = 0.93$; $\alpha = 0^o$.